Supplementary material

Dual-Stabilization Strategy Enabled High-Entropy Sulfide@Carbon Spheres for High-Performance Sodium Storage

Xinyu Liu[a,b,1], Xingbo Yu[a,b,1], Jianlong Wang[a,b], binbin Zhang[a,b], Baixin Han[a,b], Guoli Zhang[a,c,*], Kaixi Li[a,b,*] and Taotao Guan[a,b,*]

[a] *Shanxi Key Laboratory of Carbon Materials, Institute of Coal Chemistry, Chinese Academy of Sciences, Taiyuan 030001, PR China;*

[b] *Center of Materials Science and Optoelectronics Engineering, University of Chinese Academy of Sciences, Beijing 100049, PR China;*

[c] *College of Materials Science and Engineering, Taiyuan University of Technology, Taiyuan 030024, PR China;*

[1] *Xinyu Liu and Xingbo Yu contributed equally to this work.*

* Corresponding authors.

E-mail addresses: zguoli@outlook.com (G. Zhang), likx@sxicc.ac.cn (K. Li), guantt@sxicc.ac.cn (T. Guan).

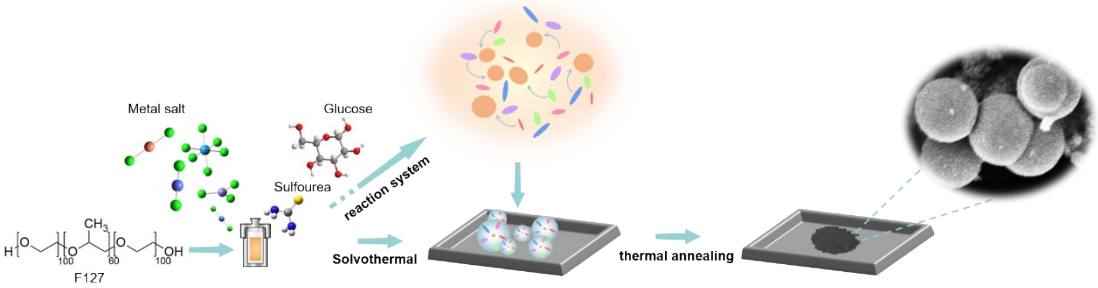

Figure S1. Schematic diagram of the preparation process for the (FeCoNiCuMo)S_2/C.

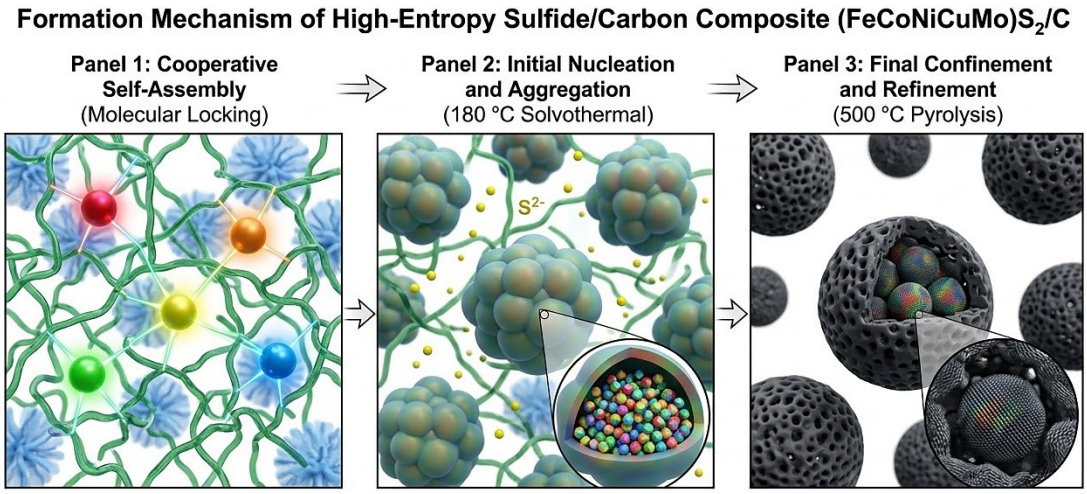

Figure S2. Schematic illustration of the multi-stage formation mechanism for (FeCoNiCuMo)S_2/C high-entropy sulfide spheres. Panel 1: Cooperative Self-Assembly (Molecular Locking). The process initiates with the formation of a stable organic–inorganic supramolecular network through hydrogen bonding between F127 surfactant micelles and glucose molecules. Simultaneously, the five transition metal cations (Fe^{2+}, Co^{2+}, Ni^{2+}, Cu^{2+}, and Mo^{5+}) are coordinated and "locked" onto the multi-dentate ligands of the polymer chains. This dual-interaction mechanism ensures an atomic-scale homogeneous distribution of the multi-element precursors, effectively preventing premature elemental segregation at the molecular level. **Panel 2: Initial Nucleation and Crystallization (180 ℃ Solvothermal Stage).** During the solvothermal reaction, the slow decomposition of thiourea provides a controlled release of S^{2-} ions. The high configurational entropy of the five-metal system (1.607R) suppresses the formation of individual binary sulfides, favoring **synchronous nuclea**tion of entropy-stabilized grains. As evidenced by Figure S12, the product at this stage consists of spherical micro-aggregates that already exhibit discernible diffraction peaks, confirming that the initial crystallization of the high-entropy sulfide core is successfully initiated during the solvothermal process. **Panel 3: Mesoscale Carbon Confinement and Structural Refinement (500 ℃ Pyrolysis).** Upon subsequent pyrolysis, the cross-linked polymer matrix is converted into a rigid and continuous carbon framework. This carbon scaffold provides intense spatial confinement that serves as a physical "cage", effectively preventing the further aggregation or long-range diffusion of the pre-formed sulfide nuclei. This mechanism strictly limits the final nanoparticle size to approximately 1 nm while facilitating the final solid-state crystallization of the dual-phase high-entropy framework, ensuring long-term structural and interfacial stability

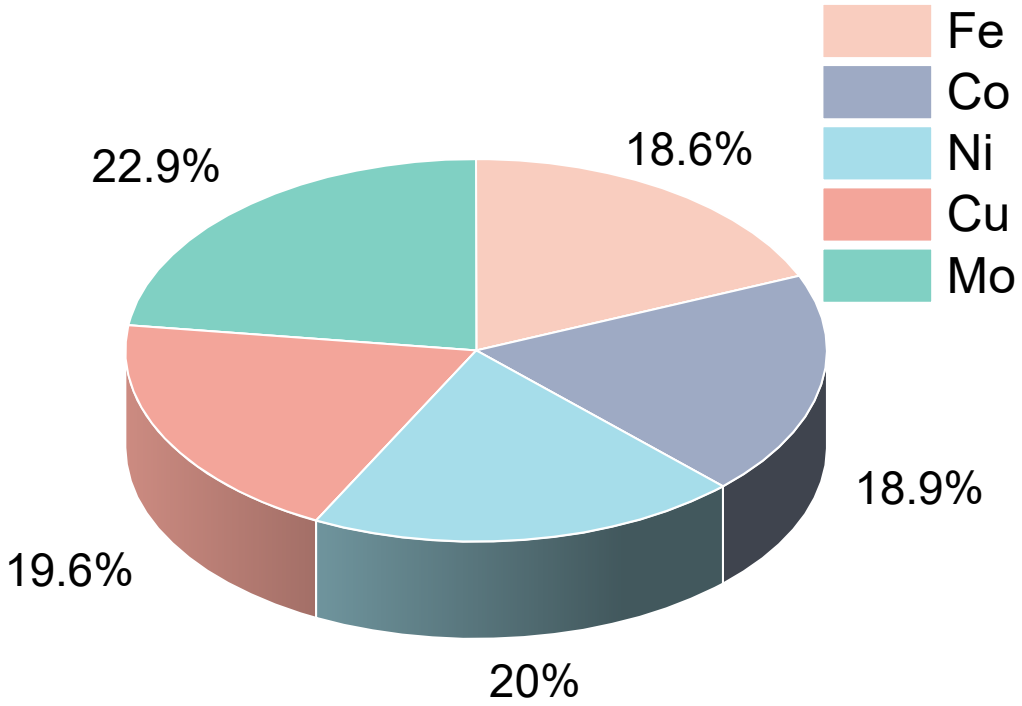

Figure S3. The ICP-OES of (FeCoNiCuMo)S_2/C

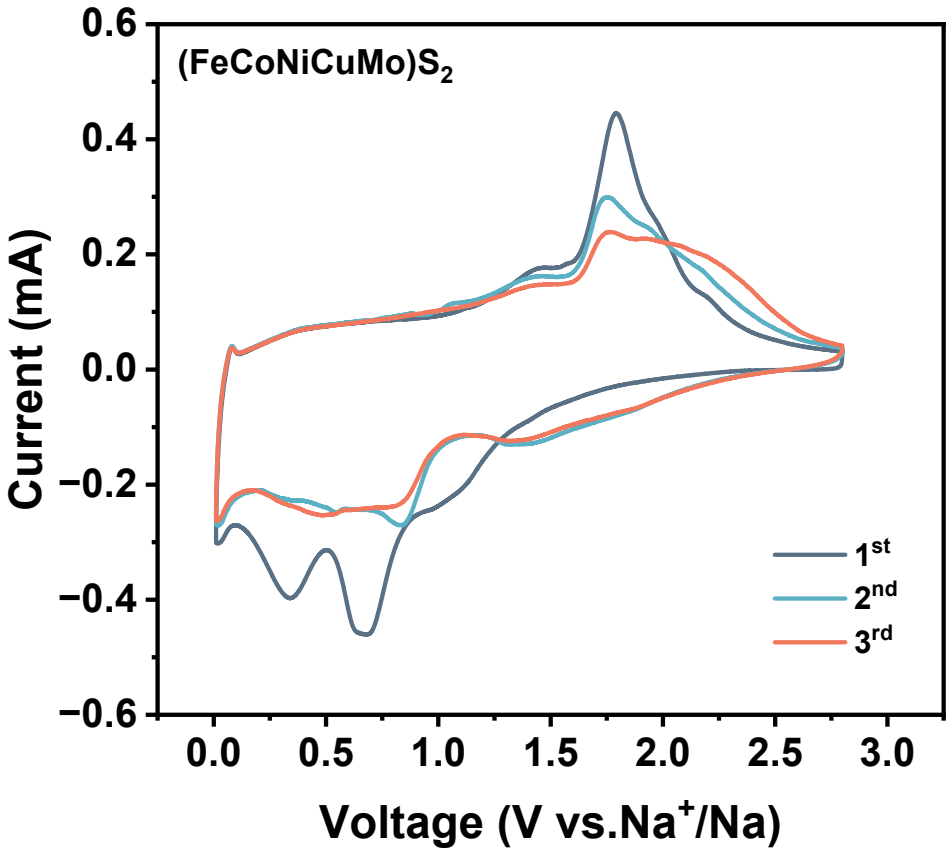

Figure S4. CV curves of $(FeCoNiCuMo)S_2$.

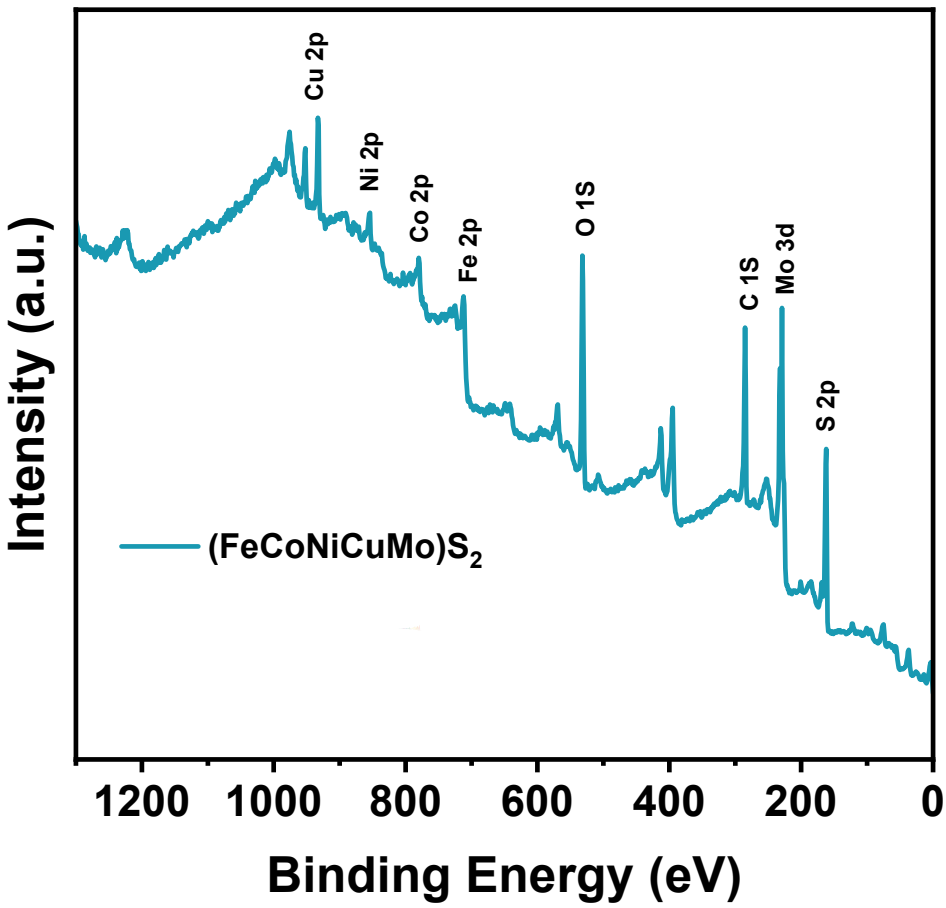

Figure S5. CV curves of (FeCoNiCuMo)S_2/C.

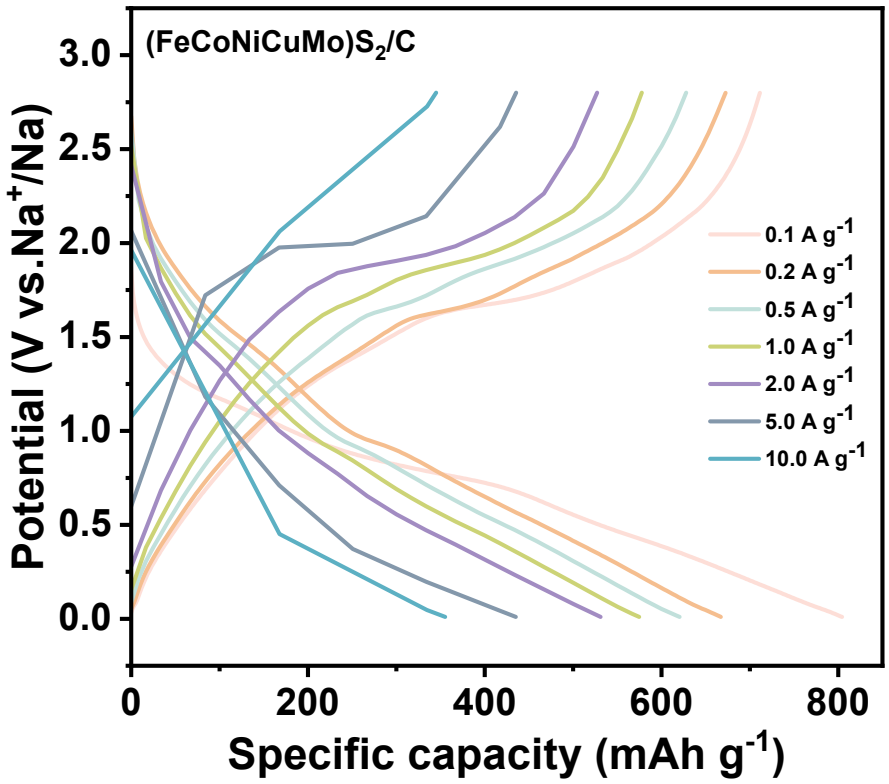

Figure S6. Rate capabilities of (FeCoNiCuMo)S_2/C.

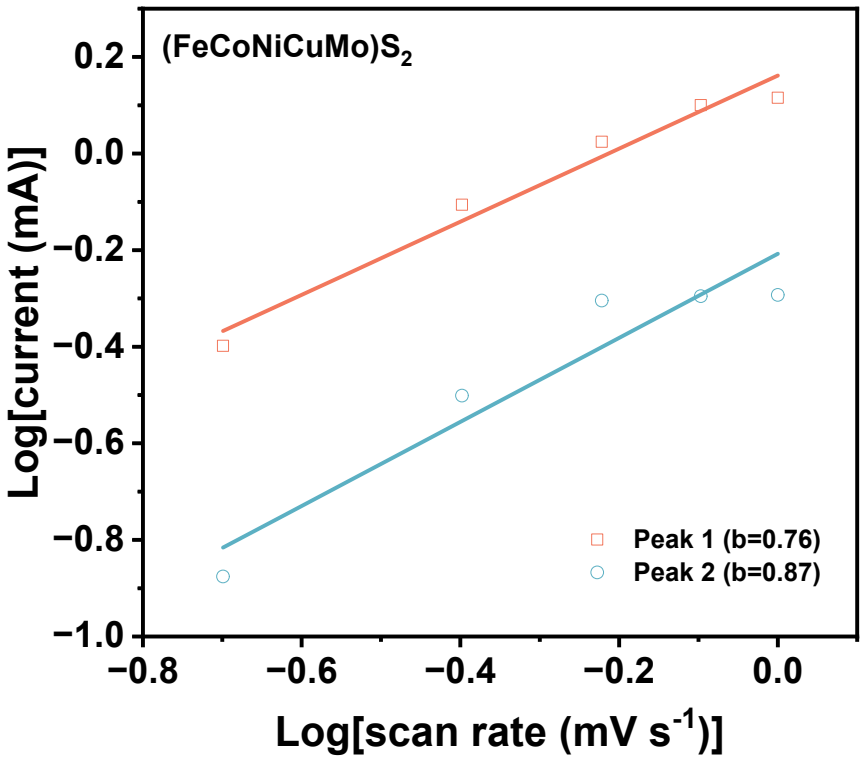

Figure S7. The linear correlation between the peak current (log i) and the sweep rate (log v) of $(FeCoNiCuMo)S_2$.

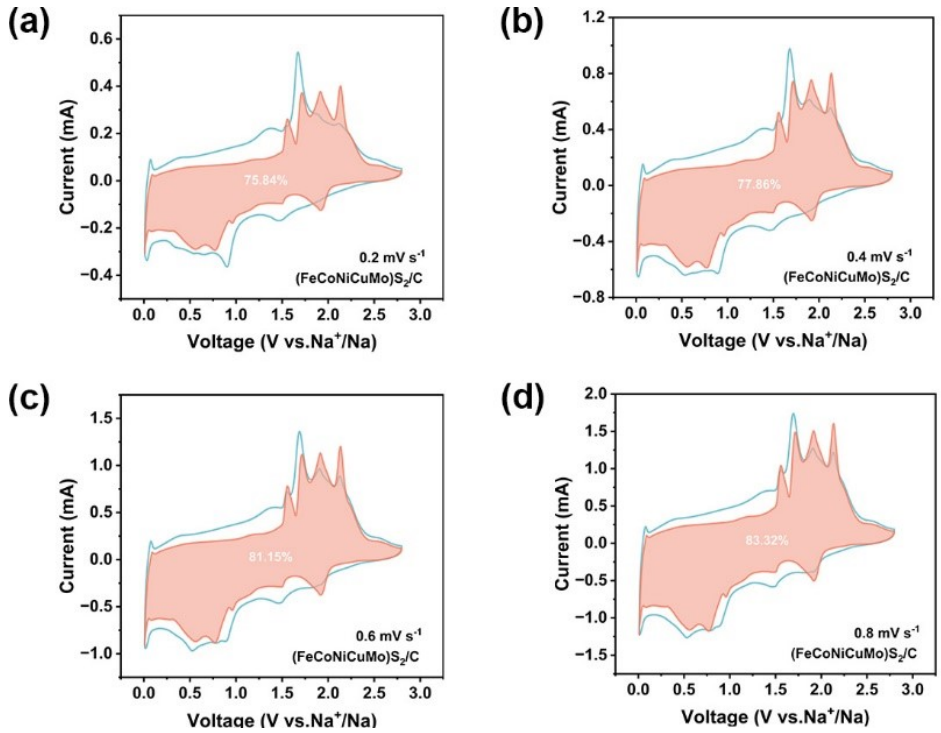

Figure S8. Capacitive contribution (shaded area) of the (FeCoNiCuMo)S_2/C electrode at scan rates of: (a) 0.2, (b) 0.4, (c) 0.6, and (d) 0.8 mV s^{-1}. Shaded areas represent capacitive contributions, with corresponding percentages labeled on each subfigure.

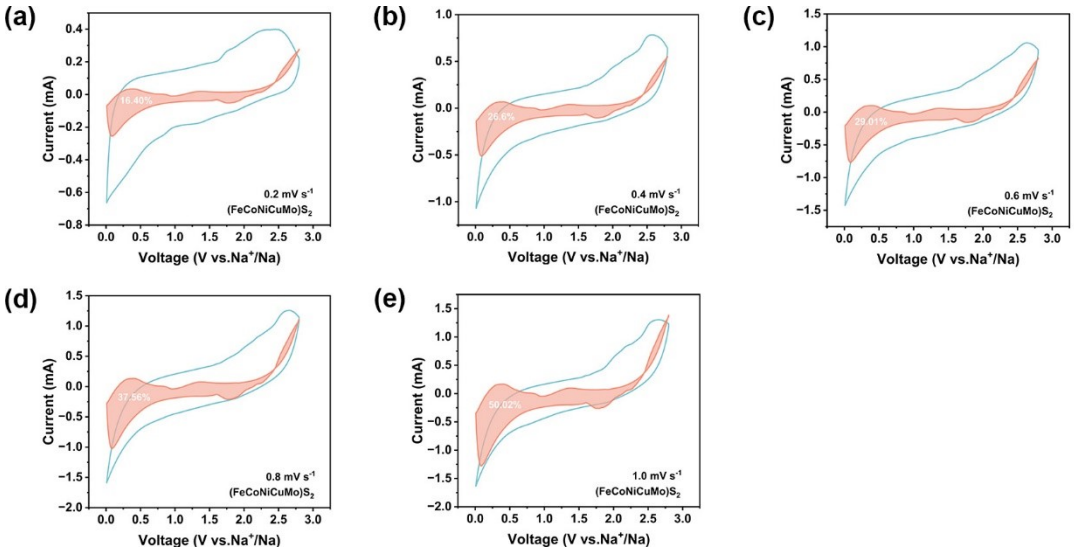

Figure S9. Capacitive contribution (shaded area) of the (FeCoNiCuMo)S_2 electrode at scan rates of: (a) 0.2, (b) 0.4, (c) 0.6, and (d) 0.8 mV s^{-1} (d) 1.0 mV s^{-1}.

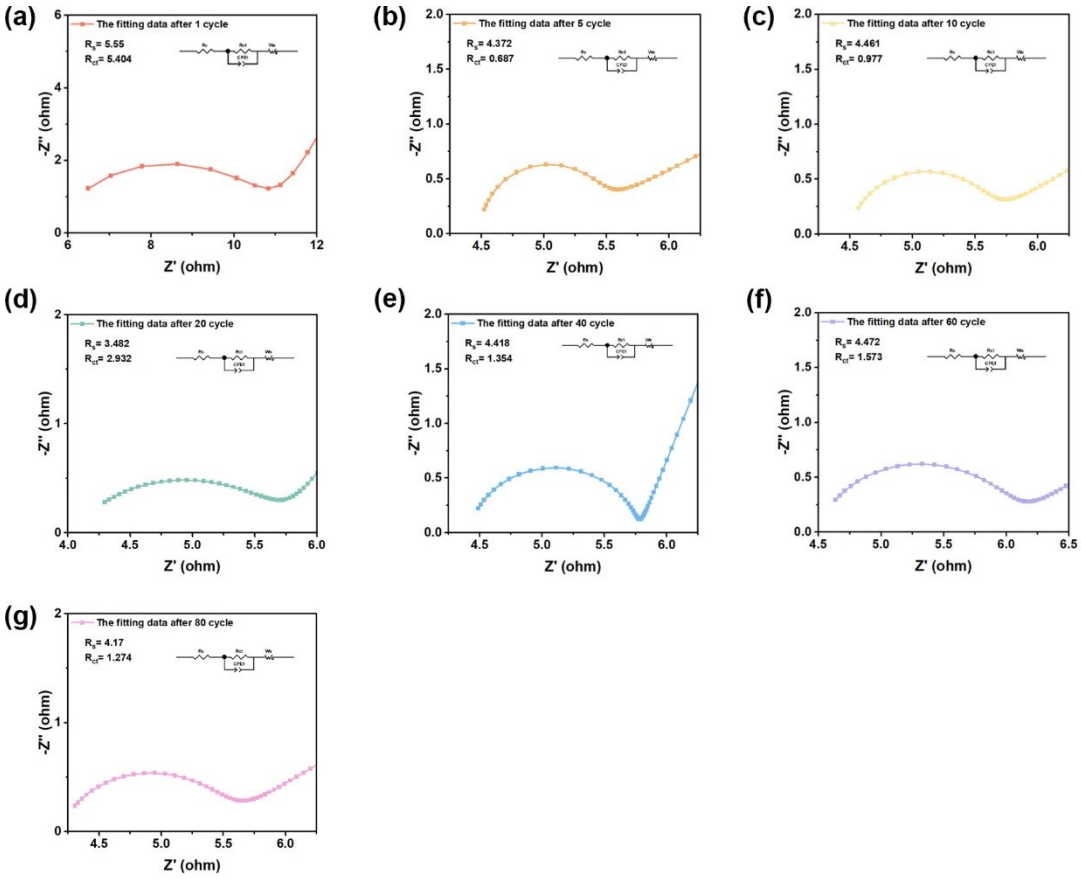

Figure S10. Electrochemical impedance spectroscopy (EIS) of the (FeCoNiCuMo)S_2/C electrode and the corresponding equivalent circuit model (inset), showing the evolution of the spectra after different numbers of charge-discharge cycles: (a) 1, (b) 5, (c) 10, (d) 20, (e) 40, (f) 60, and (g) 80 cycles.

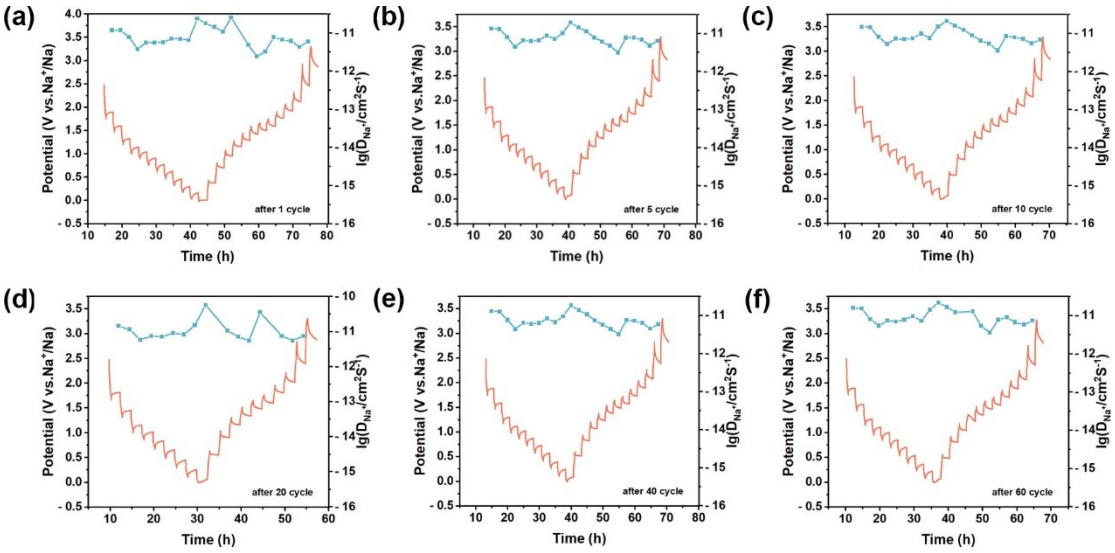

Figure S11. Potential response profiles from GITT measurements for the (FeCoNiCuMo)S_2/C electrode, showing the evolution of polarization and hysteresis upon cycling: (a) 1, (b) 5, (c) 10, (d) 20, (e) 40, and (f) 60 cycles.

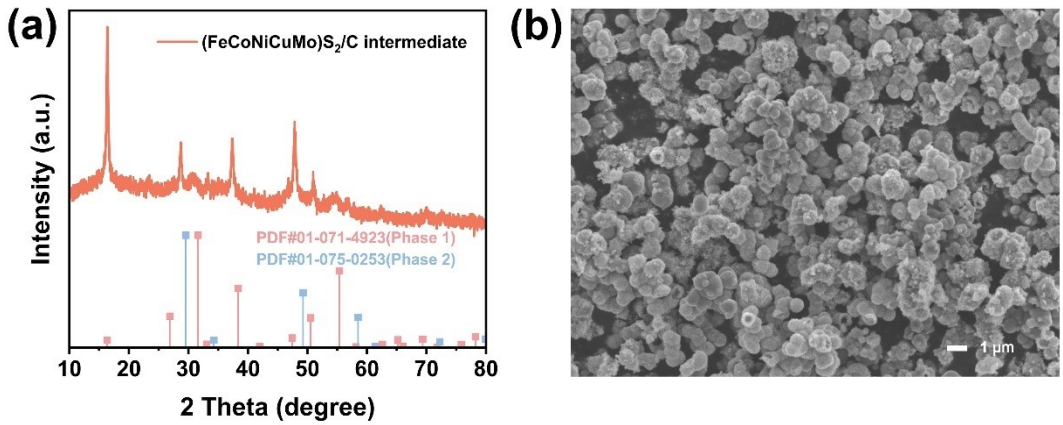

Figure S12. (a) XRD pattern and (b) SEM image of the (FeCoNiCuMo)S_2/C intermediate obtained after the solvothermal reaction.

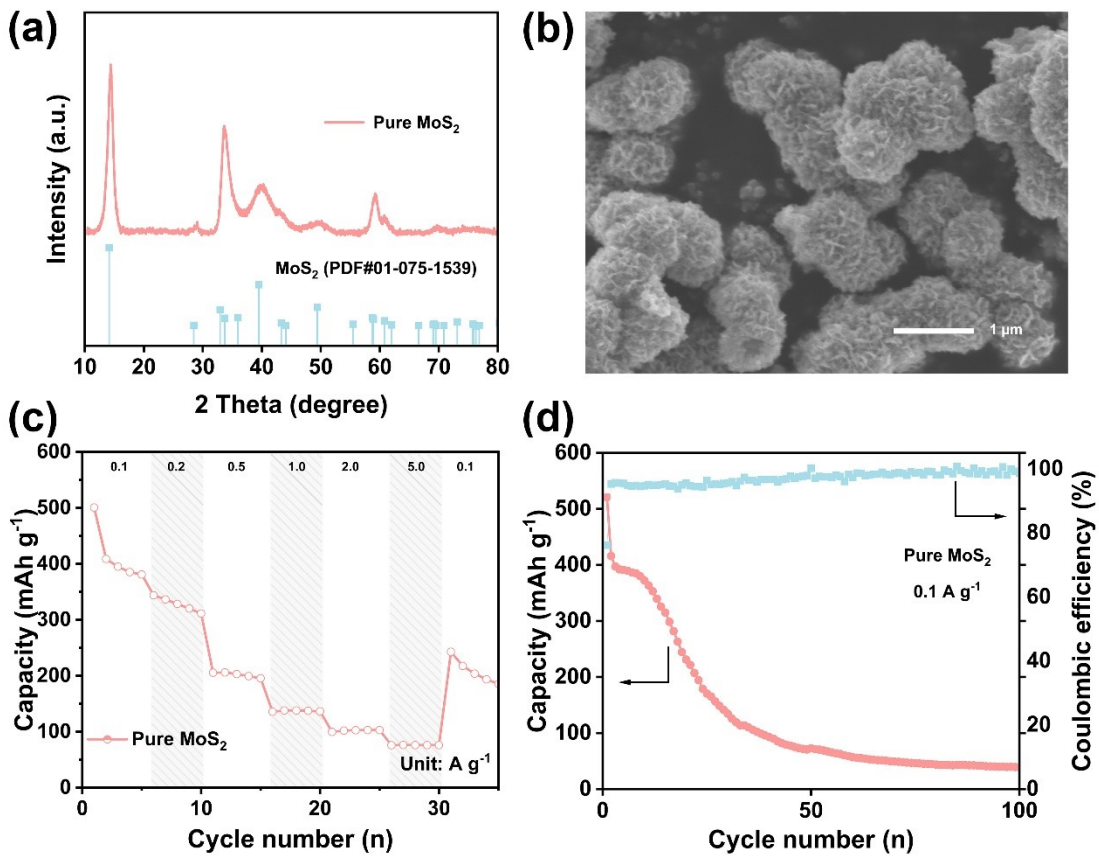

Figure S13. (a) XRD pattern and (b) SEM image of the pure MoS_2. (c) Rate capability and (d) cycling performance at 0.1 A g^{-1} of the pure MoS_2 electrode.

Table S1. The sodium storage performance of similar metal sulfides materials reported in the literature.

Samples	**Cyclic stability**			**Rate capacity**	**Ref.**
	Current density ($A\ g^{-1}$)	**Capacity ($mAh\ g^{-1}$)**	**Cycle number**		
(FeCoNiCuMo)S_2/C	**0.1**	**757**	**80**	**711,672,627,577,527, 437 and 345 mAh g^{-1} at 0.1, 0.2, 0.5, 1.0, 2.0,5.0 and 10.0 A g^{-1}, respectively**	**This Work**
	1	**468**	**600**		
SnSbMnBiTe	0.1	381.7	80	437.4, 416.5, 386.2, 381.0 and 351.0 mAh g^{-1}, at 0.2, 0.5,1.0, 2.0 and 5.0 A g^{-1}, respectively	[1]
SnCo@C	0.1	276.2	120	-	[2]
$Bi_{80}Sn_{50}Sb_{50}Cu_{80}Al_{80}$@PCFs	5	235	500	202, 190,185 and 180 mAh g^{-1} at 10, 15, 20and 25.0 A g^{-1}, respectively	[3]
NiS_2/NG	0.1	676.0	100	615.1, 594.6, 569.7, 555.8, and 545.0 mAh g^{-1} at 0.1, 0.2, 0.5, 1, 1.5, and 2.0 A g^{-1}, respectively	[4]
WZSC（WS_{2-x}/ ZnS@C）	1	329.1	500	468.2, 411.1, 352.5, 296.4, 251.4, 206.4, 180.7, and 181.9 mAh g^{-1} at 0.1, 0.2, 0.5, 1, 2, 5, 10, 20 A g^{-1}, respectively	[5]

CC-ZnS/CNT	0.1	730	200	634, 603, 522, 410, 317, and 295 mAh g^{-1} at 0.1, 0.2, 0.5, 1, 1.5, and 2 A g^{-1}, respectively	[6]
M-FeS@C+CNT.	1	366	860	505, 486, 471, 464, 454, 438, 418, 403, 380, and 332 mAh g^{-1} at 0.05, 0.1, 0.2, 0.3, 0.5, 1, 2, 3, 5, and 10 A g^{-1}, respectively	[7]
NiS_2@C@C	0.1	580.8	100	694, 671, 670, 631, 555, and 448 mAh g^{-1} at 0.05, 0.1, 0.2, 0.4, 0.8, and 1.6 A g^{-1}, respectively	[8]
Co_3S_4@PANI	0.2	252.5	100	295.5, 218.6,189.3, 184.1 mAh g^{-1} at 200, 1000, 2000, 4000 mA g^{-1}, respectively	[9]
CuS-RGO-2	0.1	392.9	50	509.1, 383.3, and 370.2 mAh g^{-1} at 100, 250, and 500 mA g^{-1}, respectively	[10]

References

[1] J. Zhao, J. Yue, S. Gao, T. Li, Synergistic Multi-Element Strategy Enables SnSbMnBiTe High-Entropy Alloy Anode for Stable and Fast Sodium Storage, ACS Sustainable Chemistry & Engineering 13(28) (2025) 11143-11152. https://doi.org/10.1021/acssuschemeng.5c04513.

[2] B. Huang, J. Yang, Y. Li, S. Xiao, Q. Chen, Carbon encapsulated Sn-Co alloy: A stabilized tin-based material for sodium storage, Materials Letters 210 (2018) 321-324. https://doi.org/10.1016/j.matlet.2017.09.055.

[3] B. Liu, M. Li, Y. Wu, R. Ren, Q. Ge, L. Fan, P. Qin, J. Qian, X. Ding, High-entropy BiSnSbCuAl nanoalloys conformed in carbon fibers as fast-charging and high-capacity anode material for sodium-ion batteries, Journal of Power Sources 652 (2025) 237600. https://doi.org/10.1016/j.jpowsour.2025.237600.

[4] S. Luo, J. Shang, Y.n. Xu, H. Cheng, L. Zhang, Y. Tang, Stabilizing NiS_2 on Conductive Component via Electrostatic Self-assembly and Covalent Bond Strategy for Promoting Sodium Storage, Advanced Functional Materials 34(39) (2024) 2403166. https://doi.org/10.1002/adfm.202403166.

[5] Y. Li, J. Qian, M. Zhang, S. Wang, Z. Wang, M. Li, Y. Bai, Q. An, H. Xu, F. Wu, L. Mai, C. Wu, Co-Construction of Sulfur Vacancies and Heterojunctions in Tungsten Disulfide to Induce Fast Electronic/Ionic Diffusion Kinetics for Sodium-Ion Batteries, Advanced Materials 32(47) (2020) 2005802. https://doi.org/10.1002/adma.202005802.

[6] T. Hou, B. Liu, X. Sun, A. Fan, Z. Xu, S. Cai, C. Zheng, G. Yu, A. Tricoli, Covalent Coupling-Stabilized Transition-Metal Sulfide/Carbon Nanotube Composites for Lithium/Sodium-Ion Batteries, ACS Nano 15(4) (2021) 6735-6746. https://doi.org/10.1021/acsnano.0c10121.

[7] H. Lim, S. Kim, J. Hoon Kim, H. Chan Lee, G. Lee, J. Hwan Park, J. Tark Han, K. Cho, Carbon shell-coated mackinawite FeS platelets as anode materials for high-performance sodium-ion batteries, Chemical Engineering Journal 458 (2023) 141354. https://doi.org/10.1016/j.cej.2023.141354.

[8] G. Zhao, Y. Zhang, L. Yang, Y. Jiang, Y. Zhang, W. Hong, Y. Tian, H. Zhao, J. Hu, L. Zhou, H. Hou, X. Ji, L. Mai, Nickel Chelate Derived NiS_2 Decorated with Bifunctional Carbon: An Efficient Strategy to Promote Sodium Storage Performance, Advanced Functional Materials 28(41) (2018) 1803690. https://doi.org/10.1002/adfm.201803690.

[9] Q. Zhou, l. Liu, Z. Huang, L. Yi, G. Cao, Co3S4@Polyaniline Nanotubes as High-Performance Anode Materials for Sodium Ion Batteries, J. Mater. Chem. A 4 (2016). https://doi.org/10.1039/C6TA01497F.

[10] J. Li, D. Yan, T. Lu, W. Qin, Y. Yao, L. Pan, Significantly Improved Sodium-Ion Storage Performance of CuS Nanosheets Anchored into Reduced Graphene Oxide with Ether-Based Electrolyte, ACS Applied Materials & Interfaces 9(3) (2017) 2309-2316. https://doi.org/10.1021/acsami.6b12529.